

# Redundant String Symmetry-Based Error Correction: Experiments on Quantum Devices

Zhangjie Qin,<sup>1,\*</sup> Daniel Azses,<sup>2,\*</sup> Eran Sela,<sup>2</sup> Robert Raussendorf,<sup>3</sup> and V. W. Scarola<sup>1</sup>

<sup>1</sup>*Department of Physics, Virginia Tech, Blacksburg, Virginia 24061, USA*

<sup>2</sup>*School of Physics and Astronomy, Tel Aviv University, Tel Aviv 6997801, Israel*

<sup>3</sup>*Institute for Theoretical Physics, Leibniz University Hannover, 30167 Hannover, Germany*

Computational power in measurement-based quantum computing (MBQC) stems from symmetry protected topological (SPT) order of the entangled resource state. But resource states are prone to preparation errors. We introduce a quantum error correction (QEC) approach using redundant non-local symmetry of the resource state. We demonstrate it within a teleportation protocol based on extending the  $\mathbb{Z}_2 \times \mathbb{Z}_2$  symmetry of one-dimensional cluster states to other graph states. Qubit ZZ-crosstalk errors, which are prominent in quantum devices, degrade the teleportation fidelity of the usual cluster state. However, as we demonstrate experimentally, once we grow graph states with redundant symmetry, perfect teleportation fidelity is restored. We identify the underlying redundant-SPT order as error-protected degeneracies in the entanglement spectrum.

**Introduction**— Measurement-based quantum computation (MBQC) is carried out purely by measurements of an entangled resource state [1–3]. Although MBQC does not use gates in the course of computation, gate errors affect resource state preparation. Thus, implementing MBQC in the current era of noisy quantum computers [4–8] requires QEC methods for MBQC. A key source of errors in quantum devices that one would like to protect against is qubit ZZ-crosstalk because it is particularly destructive [9–16].

The computational power of MBQC resource states relies on the presence of symmetries having a nontrivial action on the edge [17–23], i.e. on symmetry protected topological (SPT) order [24–34]. SPT phases can be detected by degeneracies in the entanglement spectrum or their related string order parameters (SOPs) [35–39]. In this work, we apply such a symmetry-based approach to propose a QEC method in MBQC protocols. Generally, SPT states are characterized by a certain symmetry group. As the main example on which we focus, Ref. [17, 40] proved that 1D SPT states with  $(\mathbb{Z}_2)^2$  symmetry [40] are resource states for 1D MBQC. Therefore, MBQC is immune to symmetry-preserving noises [41]. However, many common noise sources are not symmetric, e.g., ZZ-crosstalk.

Here we introduce an approach to make MBQC protocols error-oblivious by growing graph states with extended symmetry groups,  $(\mathbb{Z}_2)^g$ , where  $g$  is a graph-dependent integer. We focus on teleportation fidelity as a non-local SOP engaging all qubits in a manner similar to the SOPs underlying test for computational power [42–44]. These SOPs correspond to a path from input to output that can be tested by teleportation.

We connect these concepts with a decision triangle, Fig. 1a. Symmetry redundancy allows for multiple teleportation paths. The various errors that may occur shrink the symmetry group, but as long as a minimal amount of symmetry persists, teleportation is unaffected. After introducing the stabilizer formalism, we make this explicit in various graph states, which we also demonstrate with different numerical methods and real noisy quantum computers (IonQ and IBMQ) where we consider protection against ZZ-crosstalk and single qubit errors.

**Error-prone graph states**— Graph states are examples of SPT states. Consider a graph  $G = (V, L)$  consisting of vertices

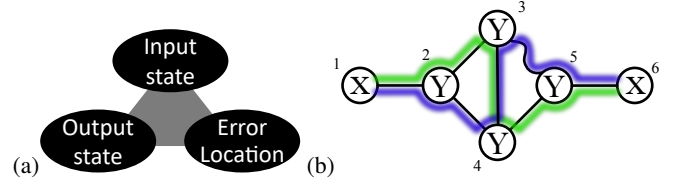


FIG. 1. (a) *Decision Triangle*: If any two items are known, our protocol reveals the third. (b) *Diamond Graph*: The simplest example of a graph state with redundant symmetry. The vertices are marked with  $X$  or  $Y$  depending on their stabilizers. The different paths, marked with blue and green, show the  $(\mathbb{Z}_2)^2 \times (\mathbb{Z}_2)^2$  symmetry, where each path contributes  $(\mathbb{Z}_2)^2$  to this redundant symmetry form. The wavy line between vertices 3 and 5 represents an idle ZZ-crosstalk error. The input (output)  $I$  ( $O$ ) is the left (right) most vertex.

$i \in V$  and links  $(i, j) \in L$ . Conventional graph states  $|\psi_G\rangle$  are the unique eigenstates of the stabilizers [45]

$$K_i = X_i \prod_{j \in \mathcal{N}(i)} Z_j, \quad (1)$$

where  $\mathcal{N}(i)$  is the neighborhood of vertex  $i$  connected to it by a link.  $X_i$  and  $Z_i$  are the usual Pauli matrices at vertex  $i$ . To create the state stabilized by the  $K_i$ 's one starts from the product state  $\prod_i |+\rangle_i$  where  $|+\rangle = (|0\rangle + |1\rangle)/\sqrt{2}$  and entangles it with the  $CZ_{ij} = e^{-i\frac{\pi}{4}(I - Z_i - Z_j + Z_i Z_j)}$  gates over all links.

Here we are concerned with the preparation of graph states on quantum computers [46, 47]. Practically, we use single qubit rotations while assuming native Ising gates

$$U_{ij}^{ZZ}(\epsilon_{ij}) = e^{-i(\pi/4 + \epsilon_{i,j})Z_i Z_j} = e^{-i(\pi/4)Z_i Z_j} E(\epsilon_{ij}), \quad (2)$$

where  $E(\epsilon_{ij}) = e^{-i\epsilon_{i,j}Z_i Z_j}$  is an idle ZZ-crosstalk error [11] parameterized by  $\epsilon_{i,j}$  that may vary from link-to-link, to prepare the state

$$|\Psi_G(\{\epsilon_{i,j}\})\rangle \equiv \prod_{i,j \in L} U_{ij}^{ZZ}(\epsilon_{i,j}) \left[ \prod_{i \in V} e^{i\theta_i Z_i} |+\rangle_i \right], \quad (3)$$

where the  $\theta_i$ 's depend on the graph structure. For example we consider the diamond graph in Fig. 1b. It contains an input and output vertex, 1 and 6, respectively.

In our convention, adapted for native Ising gates, ideal graph states,  $|\Psi_G(\{\epsilon_{i,j} = 0\})\rangle$ , are stabilizer states with a minor modification: some vertices contain an additional  $e^{-i\frac{\pi}{4}Z_i}$  rotation, thus the stabilizers at these vertices are replaced by  $K_i = Y_i \prod_{j \in \mathcal{N}(i)} Z_j$ . We mark those vertices in the figures by  $Y$  instead of  $X$  for the usual vertices.

*SPT phase and teleportation*— To test if the teleportation property of a resource state  $|\psi_G\rangle$  is protected against a unitary perturbation such as  $E(\epsilon_{ij})$  we first introduce the symmetries  $\{s_\alpha\}$  which generate the symmetry group of the graph,  $\mathcal{S}$ , i.e.  $s_\alpha |\psi_G\rangle = |\psi_G\rangle$  for any  $s_\alpha \in \mathcal{S}$ . Each symmetry is a Pauli string generated by the stabilizers

$$s_\alpha \equiv \prod_{j \in \alpha} K_j, \quad (4)$$

where  $\alpha$  denotes a subset of the vertices which can be non-local. Each symmetry can be factorized into parts acting on the input, middle, and output, as  $s_\alpha = s_\alpha^{(I)} s_\alpha^{(M)} s_\alpha^{(O)}$ . By measuring the middle region in the Pauli basis according to  $s_\alpha^{(M)}$ , the operator is transformed to a sign  $\pm 1$  depending on the measurement results. We assume that a simultaneous measurement exists implying  $s_\alpha^{(M)}$  commute for different  $\alpha$ . Finally there should be at least two such symmetries, such that the common eigenstate of both  $s_\alpha^{(I)} s_\alpha^{(O)}$  ( $\alpha = x, z$ ) is a maximally entangled Bell state between the input and output.

This can be exemplified for the 1D chain graph. For illustration we consider a 6-qubit example. It has an odd and even symmetry generators  $s_{\text{odd}} = s_{135} = X_1 Y_3 Y_5 Z_6$  and  $s_{\text{even}} = s_{246} = Z_1 Y_2 Y_4 X_6$ , thus  $\mathcal{S} = \mathbb{Z}_2 \times \mathbb{Z}_2$ . All the  $s_\alpha^{(M)}$  involve only Pauli- $Y$  operators hence they commute. By measuring all the middle qubits in the  $x$ -basis we obtain a Bell state between the input and output qubits. Therefore, this state is a resource state for general 1-qubit MBQC. As in this example, one can always write [2]  $s_x^{(I)} = X_I$ ,  $s_z^{(I)} = Z_I$  and  $s_x^{(O)} = U(X_O)$ ,  $s_z^{(O)} = U(Z_O)$  for some unitary  $U$  which does not change the entanglement of the Bell state, where  $U(O) = UOU^\dagger$ .

Consider an error described by a unitary operator  $E$  affecting the resource state,  $|\Psi'_G\rangle = E|\Psi_G\rangle$ . As long as  $E$  commutes with  $\mathcal{S}$ , it does not alter the relation  $s_\alpha |\Psi'_G\rangle = |\Psi'_G\rangle$ , and hence the perfect teleportation property persists [41]. This property defines computational power, in this case of teleportation, of the SPT phase of which the unperturbed chain graph state is a specific state. However, perturbations such as  $E_{ij}^{ZZ}(\epsilon_{i,i+1})$  on the chain graph state do not commute with these symmetries in general (unless the idle  $ZZ$ -crosstalk acts only on even spaced vertices  $j - i = 2m$ , where  $m \in \mathbb{N}$ ). Is it possible to restore perfect teleportation in the presence of such non-symmetric perturbations?

*Redundant symmetry*— Our central idea is to work with a graph having an extended symmetry group, beyond the one absolutely required for computational power. Starting from such a higher symmetry, consider the symmetry subgroup  $\mathcal{S}^{(E)}$  which commutes with a perturbation  $E$ , i.e.  $[E, s_\alpha] = 0$  for any  $s_\alpha \in \mathcal{S}^{(E)}$ . If this subgroup contains  $(\mathbb{Z}_2)^2$  as a

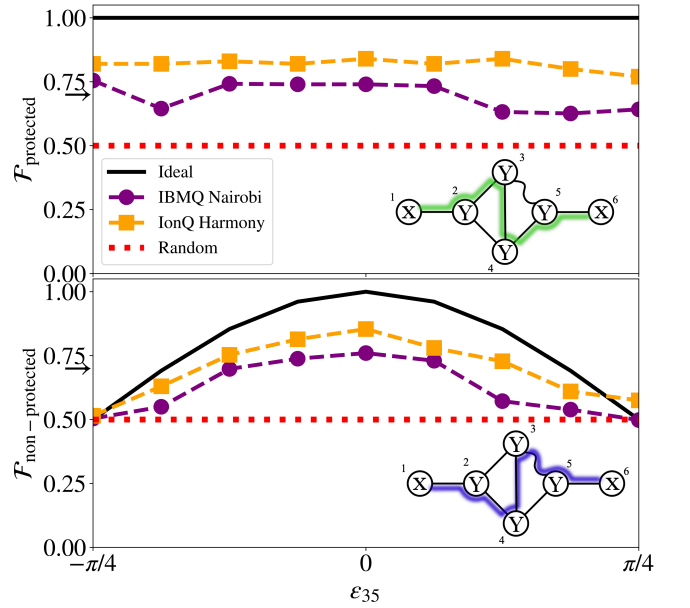


FIG. 2. Fidelity for teleportation in the self-loop diamond graph along a preserved (top) and broken (bottom) symmetry path plotted as a function of the perturbation strength to the native Ising gates. The solid line in the top panel indicates perfect transmission due to topological symmetry protection in the absence of other noise sources. Square (Circle) data are obtained from IonQ (IBMQ) quantum devices. These data are lower than unity due to noise sources unprotected by topological symmetry, e.g., two-qubit depolarizing noise [48]. The arrow at  $2/3$  shows the threshold above which transmission along a quantum channel is guaranteed. The dotted line at  $1/2$  indicates a random classical channel.

subgroup, then the computational power persists in the presence of this perturbation. This protection holds for different perturbations  $E_i$  that may happen one at a time, even if  $\mathcal{S}^{(E_i)}$  are different, as long as they all contain  $(\mathbb{Z}_2)^2$ . Furthermore, these sub-group symmetries generate a nontrivial redundancy if they share one or more vertices besides  $I$  and  $O$ . Many sub-group symmetries can be found to commute for Ising-based graphs [Eq. (3)] since link operators of the form  $\{I_i I_j, X_i X_j, Y_i Y_j, Z_i Z_j\}$  all commute on the same link.

To demonstrate symmetry-redundant QEC consider the diamond graph with a preparation  $ZZ$ -crosstalk error, e.g., between qubits 3 and 5 as marked by a wavy line in Fig. 1b. The unperturbed graph state has a higher symmetry compared to the 1D chain graph. This can be understood geometrically by considering two entwined paths connecting the input and output qubits, see the green and blue paths in Fig. 1. The blue path allows introduction of one pair of even and odd symmetries,  $s_{135} = X_1 X_3 X_5 Z_6$  and  $s_{246} = Z_1 X_2 X_4 X_6$ . However, the green path allows introduction of another pair of even and odd symmetries,  $s_{145} = X_1 X_4 X_5 Z_6$  and  $s_{236} = Z_1 X_2 X_3 X_6$ . The total symmetry group is thus  $(\mathbb{Z}_2)^4$ . It is convenient to label the symmetries as  $(p, q)$  according to the

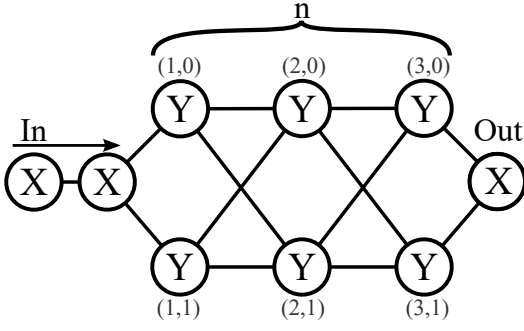


FIG. 3. *Hourglass Graph*: Another example graph with redundant SPT symmetry wherein any 1-qubit error in one bulk link is obliviously correctable, but also identifiable. Moreover, in this graph we can correct errors on many vertices given that at least one path remains from the input to the output.  $n$  labels the bulk length and is set to  $n = 3$  for this example.

two symmetries  $q = x, z$  corresponding to each path  $p$ ,

$$\begin{aligned} s_{p,x} &= X_I s_{p,x}^{(M)} U(X_O), \\ s_{p,z} &= Z_I s_{p,x}^{(M)} U(Z_O), \end{aligned} \quad (5)$$

where we have  $I = 1$ ,  $O = 6$ ,  $U$  is the Haddamard matrix,  $s_{1,x} = s_{135}$ ,  $s_{1,z} = s_{246}$ ;  $s_{2,x} = s_{145}$  and  $s_{2,z} = s_{236}$ .

Let us observe how ZZ-crosstalk affects the computational power and demonstrate ‘error oblivious’ teleportation using  $\mathbb{Z}_2^4$  SPT order. The perturbation  $\epsilon_{i,j}$  commutes only with the  $p = 2$  [ $p = 1$ ] symmetries for crosstalk on links  $(i, i + 2)$  for  $i = 2, 3$  [ $(i, i + 1)$  for  $i = 2, 4$ ]. For example, the  $\epsilon_{35}$  error in Fig. 1b commutes only with  $\{s_{135}, s_{246}\}$ , i.e. the symmetries corresponding to path  $p = 1$ . This is sufficient to guarantee perfect teleportation fidelity.

To demonstrate teleportation robustness, we prepare qubit 1 in state  $|\phi_I^{\hat{r}}\rangle$ , where the unit vector  $\hat{r}$  corresponds to a location on the Bloch sphere. Quantum teleportation can be seen as an identity gate in MBQC as the output state is the same as the input  $\phi_O^{\hat{r}} = \phi_I^{\hat{r}}$ , where the state corresponds to a unit vector  $\hat{r}$  on the Bloch sphere. Single-qubit measurements on input and bulk qubits (1-5 in Fig. 1b) teleport information from the graph input to the output [1, 2, 49–51]. The success of the teleportation is measured by the fidelity  $\mathcal{F}_{\hat{r}} \equiv |\langle \phi_I^{\hat{r}} | U_{\Sigma} | \phi_O^{\hat{r}} \rangle|^2$ , which compares the input qubit state  $\phi_I^{\hat{r}}$  to the output qubit state  $\phi_O^{\hat{r}}$  [See Ref. 48 for a generalized fidelity]. The byproduct operator  $U_{\Sigma}$  depends on measurement outcomes and is defined in Ref. 48. In the following we present quantum device results for  $\mathcal{F} = \mathcal{F}_{\hat{z}}$  but we have obtained the same qualitative results for other  $\hat{r}$ .

Figure 2 plots the fidelity for the ideal case and for two quantum devices. Ideally we have perfect teleportation,  $\mathcal{F} = 1$  in the top panel. Assuming ZZ perturbations  $\epsilon_{i,j}$  act on no more than one symmetry path corresponding to unknown outer links of the diamond, the redundant paths protect the perfect teleportation protocol as one  $(\mathbb{Z}_2)^2$  symmetry remains, though determining which symmetry is left unbroken requires post processing [48]. We check that the non-trivial SPT nature

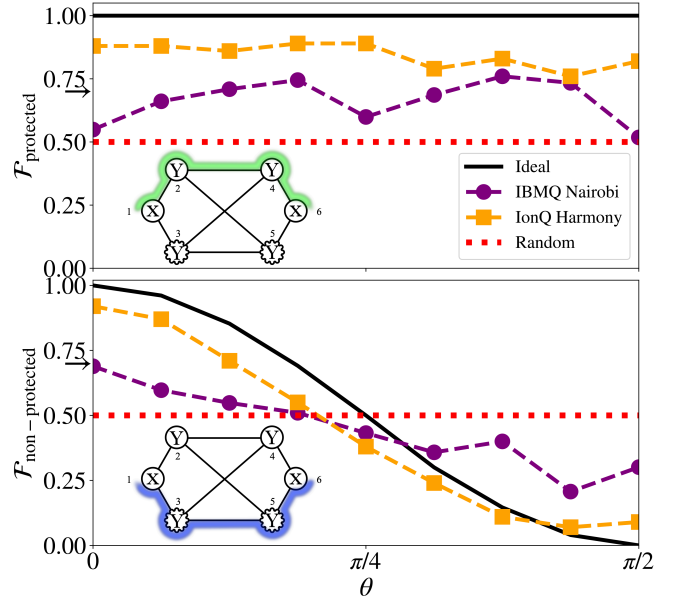


FIG. 4. The same as Fig. 2 but for the hourglass graph with  $n = 2$  and single qubit errors,  $e^{-i\theta(X_{1,1} + X_{2,1})/2}$ , indicated by wavy lines on bottom vertices. The top panel shows evidence of teleportation across a quantum channel protected by the upper non-local string symmetry in both quantum devices (insets)

exists in the unbroken symmetry by computing the eigenvalues of the reduced density matrix [48].

Figure 2 shows that for both quantum devices the teleportation is not perfect due to noise which is excluded in our symmetry analysis. Nonetheless, the graph state entanglement is ensured to allow transmission across a quantum channel [52–56] if  $\mathcal{F}_{\hat{r}} > 2/3$ . For  $2/3 \geq \mathcal{F}_{\hat{r}} > 1/2$ , the channel could be either quantum or classical. For  $\mathcal{F}_{\hat{r}} \leq 1/2$ , entanglement in the graph state has degraded to a point where there is only a classical channel. We are able to reproduce the observed fidelity trend for the IonQ device using a two-qubit depolarizing noise model. Ref. 48 discusses the modeling and other noise sources for the quantum devices.

The diamond graph illustrates the transport of quantum information over redundantly many paths. Yet it can not correct errors on any link, e.g.,  $\epsilon_{34}$ , and is limited to ZZ, XX or YY link errors. However, here we assumed that only one such crosstalk event took place. In the case of simultaneous crosstalk on both paths, the redundant-SPT order does not protect information flow. Furthermore, in MBQC one has to apply byproduct operators depending on the measurement outcome. The byproduct operator depends on the path. Thus, one needs to know the path through which the information was transmitted. This can be done by a calibration process according to the error-tomography with the decision triangle, Fig. 1a. Below we discuss a generalization that deals with these issues.

*Hourglass Graph*—One possible generalization of the diamond graph to many qubits is the hourglass graph shown in

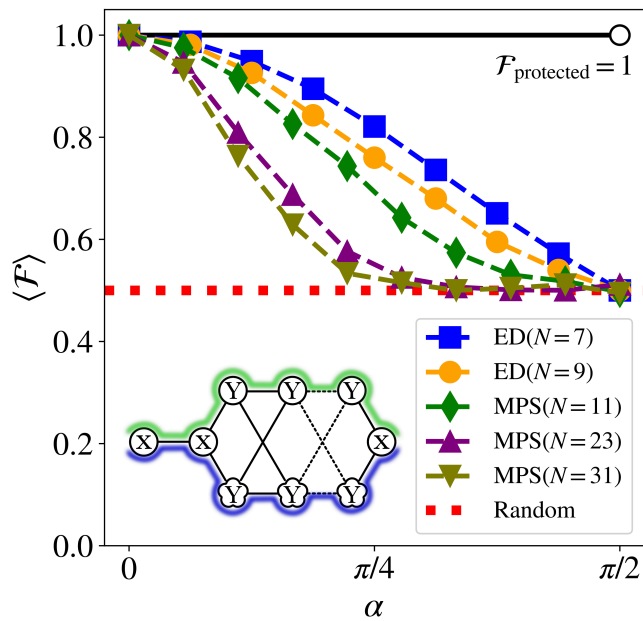


FIG. 5. Teleportation fidelity versus  $Z$ -perturbation strength in the hourglass graph [Eq. (6)] averaged over several different input qubit orientations. The solid line shows perfect teleportation along the upper path obtained for all system lengths for all but the  $\alpha = \pi/2$  point. The symbols, obtained using exact diagonalization (ED) and MPS, are for various graph lengths,  $N = 2n + 3$  (See Fig. 3). Teleportation along the perturbed path degrades with increasing graph length.

Fig. 3. As we will show, it protects MBQC teleportation from any unitary perturbation in several bulk links or vertices. As in the diamond graph, one has several routes of information from input to output. However, in this case the number of paths grows exponentially with the length of the bulk,  $n$ . For each additional two vertices in the bulk, the number of paths multiplies to yield  $2^n$  possible paths. Assuming an error happened on some known link, we are left with  $3 \times 2^{n-2}$  paths, as 3 links survived from the 4 near the link position, that still convey the information as their symmetries are left unchanged and commute with the broken links. Further assuming an error on a link that removes both sites at its endpoints we are left with  $2^{n-2}$  paths, as for each erroneous qubit we lose half of the paths. Similarly, 1-qubit error reduces half of paths to  $2^{n-1}$ . However, one needs to find the broken link in order to select the correct byproduct operators of one or more non-corrupted paths. To know which path has not been corrupted by an error, we construct a post-processing calibration protocol [48].

Figure 4 shows fidelity for the hourglass graph state with errors applied to lower vertices.  $n = 2$  was chosen to fit the graph on quantum devices. A comparison of top and bottom panels shows that post processing leveraging the intact symmetry group (top panel with  $\mathcal{F} > 2/3$ ) allows teleportation along a quantum channel for both quantum devices.

We have also tested our protocol on large  $n$  using classical

exact diagonalization and Matrix Product State (MPS) simulations [57–63]. We consider a case with perturbations that explicitly break many of the string symmetries (Ref. 48 discusses SOPs and the symmetry-preserving case).

We consider the Hamiltonian:

$$H_X = -\cos \alpha \sum_{j=1}^N K_j - \sin \alpha \sum_{i=1}^n Z_{i,1}, \quad (6)$$

where  $\alpha = 0$  yields the ideal hourglass graph state as the ground state and  $\pi/2 > \alpha > 0$  adds non-symmetric perturbations to the lower sites of the hourglass graph. The black line in Figure 5 plots perfect fidelity arising from teleportation along the upper path. The remaining lines show the degradation in teleportation fidelity when using the lower path arising from broken string order. These classical simulations show that large  $n$  still permits perfect transmission along the graph in spite of large numbers of non-symmetry preserving errors in the graph.

*Summary and Outlook*— We constructed an error correction and detection protocol using non-local symmetries in graph states. By showing that certain graph states contain enlarged  $(\mathbb{Z}_2)^g$  SPT order we used the ensuing redundancy in symmetry to locate and correct errors. The protocol was demonstrated to protect non-local measurement-based teleportation along a quantum channel in quantum devices for example graphs.

Our work has important implications for correcting errors in MBQC resource states on noisy near-term quantum computers where  $ZZ$ -crosstalk is non-trivial to correct using conventional error correction with local stabilizers. Furthermore, our protocol can be extended beyond teleportation to correct other logical operations. We also note that our work has applications to low-overhead correction of error-prone quantum networks.

We acknowledge support from ARO W911NF2010013. ES acknowledges support from the European Research Council (ERC) Synergy funding for Project No. 951541, and the Israel Science Foundation, grant number 154/19. RR is funded by NSERC. VWS and ZQ acknowledge support from AFOSR (FA2386-21-1-4081, FA9550-23-1-0034, A9550-19-1-0272) and ARO W911NF2210247. We acknowledge use of the IBM quantum cloud experience and IonQ for this work. The views expressed are those of the authors and do not reflect the official policy or position of IBM, the IBMQ team, or IonQ.

\* These authors contributed equally to this work.

- [1] R. Raussendorf and H. J. Briegel, A one-way quantum computer, *Phys. Rev. Lett.* **86**, 5188 (2001).
- [2] R. Raussendorf, D. E. Browne, and H. J. Briegel, Measurement-based quantum computation on cluster states, *Phys. Rev. A* **68**, 022312 (2003).
- [3] H. J. Briegel and R. Raussendorf, Persistent entanglement in arrays of interacting particles, *Phys. Rev. Lett.* **86**, 910 (2001).

- [4] J. Preskill, Quantum computing in the NISQ era and beyond, *Quantum* **2**, 79 (2018).
- [5] A. Y. Kitaev, Quantum communication, computing, and measurement, in *Proceedings of the 3rd International Conference of Quantum Communication and Measurement* (New York: Plenum, 1997).
- [6] M. A. Nielsen and I. L. Chuang, *Quantum Computation and Quantum Information: 10th Anniversary Edition* (Cambridge University Press, 2010).
- [7] A. Y. Kitaev, Fault-tolerant quantum computation by anyons, *Ann. Phys.* **303**, 2 (2003).
- [8] A. R. Calderbank, E. M. Rains, P. W. Shor, and N. J. A. Sloane, Quantum error correction via codes over  $gf(4)$  (1997), arXiv:quant-ph/9608006.
- [9] L. Dicarlo, J. M. Chow, J. M. Gambetta, L. S. Bishop, B. R. Johnson, D. I. Schuster, J. Majer, A. Blais, L. Frunzio, S. M. Girvin, and R. J. Schoelkopf, Demonstration of two-qubit algorithms with a superconducting quantum processor, *Nature* **460**, 240 (2009).
- [10] D. C. McKay, S. Sheldon, J. A. Smolin, J. M. Chow, and J. M. Gambetta, Three-qubit randomized benchmarking, *Phys. Rev. Lett.* **122**, 200502 (2019).
- [11] M. Sarovar, T. Proctor, K. Rudinger, K. Young, E. Nielsen, and R. Blume-Kohout, Detecting crosstalk errors in quantum information processors, *Quantum* **4**, 321 (2020).
- [12] T. Cai, X. Han, Y. Wu, Y. Ma, J. Wang, Z. Wang, H. Zhang, H. Wang, Y. Song, and L. Duan, Impact of spectators on a two-qubit gate in a tunable coupling superconducting circuit, *Phys. Rev. Lett.* **127**, 060505 (2021).
- [13] I. Heinz and G. Burkard, Crosstalk analysis for single-qubit and two-qubit gates in spin qubit arrays, *Phys. Rev. B* **104**, 045420 (2021).
- [14] D. W. Kanaar, U. Güngördü, and J. P. Kestner, Two-qubit controlled-Z gates robust against charge noise in silicon while compensating for crosstalk using neural network, *Phys. Rev. B* **105**, 245308 (2022).
- [15] L. Xie, J. Zhai, Z. Zhang, J. Allcock, S. Zhang, and Y.-C. Zheng, Suppressing ZZ crosstalk of quantum computers through pulse and scheduling co-optimization, in *Proceedings of the 27th ACM International Conference on Architectural Support for Programming Languages and Operating Systems* (ACM, 2022).
- [16] Z. Ni, S. Li, L. Zhang, J. Chu, J. Niu, T. Yan, X. Deng, L. Hu, J. Li, Y. Zhong, S. Liu, F. Yan, Y. Xu, and D. Yu, Scalable method for eliminating residual ZZ interaction between superconducting qubits, *Phys. Rev. Lett.* **129**, 040502 (2022).
- [17] D. V. Else, I. Schwarz, S. D. Bartlett, and A. C. Doherty, Symmetry-protected phases for measurement-based quantum computation, *Phys. Rev. Lett.* **108**, 240505 (2012).
- [18] J. Miller and A. Miyake, Latent computational complexity of symmetry-protected topological order with fractional symmetry, *Phys. Rev. Lett.* **120**, 170503 (2018).
- [19] J. Miller and A. Miyake, Hierarchy of universal entanglement in 2d measurement-based quantum computation, *npj Quantum Inf.* **2**, 1 (2016).
- [20] A. Miyake, Quantum computation on the edge of a symmetry-protected topological order, *Phys. Rev. Lett.* **105**, 040501 (2010).
- [21] R. Raussendorf, C. Okay, D.-S. Wang, D. T. Stephen, and H. P. Nautrup, Computationally universal phase of quantum matter, *Phys. Rev. Lett.* **122**, 090501 (2019).
- [22] D. T. Stephen, H. P. Nautrup, J. Bermejo-Vega, J. Eisert, and R. Raussendorf, Subsystem symmetries, quantum cellular automata, and computational phases of quantum matter, *Quantum* **3**, 142 (2019).
- [23] D. Azses, D. F. Mross, and E. Sela, Symmetry-resolved entanglement of two-dimensional symmetry-protected topological states, *Physical Review B* **107**, 115113 (2023).
- [24] X.-G. Wen, Colloquium: Zoo of quantum-topological phases of matter, *Rev. Mod. Phys.* **89**, 041004 (2017).
- [25] X. Chen, Z.-C. Gu, and X.-G. Wen, Local unitary transformation, long-range quantum entanglement, wave function renormalization, and topological order, *Phys. Rev. B* **82**, 155138 (2010).
- [26] X. Chen, Z.-C. Gu, Z.-X. Liu, and X.-G. Wen, Symmetry protected topological orders and the group cohomology of their symmetry group, *Phys. Rev. B* **87**, 155114 (2013).
- [27] X. Chen, Z.-C. Gu, and X.-G. Wen, Complete classification of one-dimensional gapped quantum phases in interacting spin systems, *Phys. Rev. B* **84**, 235128 (2011).
- [28] A. Y. Kitaev, Unpaired majorana fermions in quantum wires, *Physics-Usppekhi* **44**, 131 (2001).
- [29] J. E. Moore and L. Balents, Topological invariants of time-reversal-invariant band structures, *Phys. Rev. B* **75**, 121306 (2007).
- [30] M. Oshikawa, Hidden  $\mathbb{Z}_2 \times \mathbb{Z}_2$  symmetry in quantum spin chains with arbitrary integer spin, *J. Condens. Matter Phys.* **4**, 7469 (1992).
- [31] D. Pérez-García, M. M. Wolf, M. Sanz, F. Verstraete, and J. I. Cirac, String order and symmetries in quantum spin lattices, *Phys. Rev. Lett.* **100**, 167202 (2008).
- [32] F. Pollmann, E. Berg, A. M. Turner, and M. Oshikawa, Symmetry protection of topological phases in one-dimensional quantum spin systems, *Phys. Rev. B* **85**, 075125 (2012).
- [33] S. Ryu, A. P. Schnyder, A. Furusaki, and A. W. Ludwig, Topological insulators and superconductors: tenfold way and dimensional hierarchy, *New J. Phys.* **12**, 065010 (2010).
- [34] T. Senthil, Symmetry-protected topological phases of quantum matter, *Annu. Rev. Condens. Matter Phys.* **6**, 299 (2015).
- [35] F. Pollmann, A. M. Turner, E. Berg, and M. Oshikawa, Entanglement spectrum of a topological phase in one dimension, *Phys. Rev. B* **81**, 064439 (2010).
- [36] A. M. Turner, F. Pollmann, and E. Berg, Topological phases of one-dimensional fermions: An entanglement point of view, *Phys. Rev. B* **83**, 075102 (2011).
- [37] K. Choo, C. W. von Keyserlingk, N. Regnault, and T. Neupert, Measurement of the entanglement spectrum of a symmetry-protected topological state using the ibm quantum computer, *Phys. Rev. Lett.* **121**, 086808 (2018).
- [38] E. Cornfeld, L. A. Landau, K. Shtengel, and E. Sela, Entanglement spectroscopy of non-abelian anyons: Reading off quantum dimensions of individual anyons, *Phys. Rev. B* **99**, 115429 (2019).
- [39] D. Azses and E. Sela, Symmetry-resolved entanglement in symmetry-protected topological phases, *Phys. Rev. B* **102**, 235157 (2020).
- [40] W. Son, L. Amico, and V. Vedral, Topological order in 1d cluster state protected by symmetry, *Quantum Inf. Process.* **11**, 1961 (2011).
- [41] D. Azses, R. Haenel, Y. Naveh, R. Raussendorf, E. Sela, and E. G. Dalla Torre, Identification of symmetry-protected topological states on noisy quantum computers, *Phys. Rev. Lett.* **125**, 120502 (2020).
- [42] R. Raussendorf, W. Yang, and A. Adhikary, Measurement-based quantum computation in finite one-dimensional systems: string order implies computational power, arXiv:2210.05089 (2022).
- [43] R. Raussendorf, D.-S. Wang, A. Prakash, T.-C. Wei, and D. T.

- Stephen, Symmetry-protected topological phases with uniform computational power in one dimension, *Phys. Rev. A* **96**, 012302 (2017).
- [44] J. Miller and A. Miyake, Resource quality of a symmetry-protected topologically ordered phase for quantum computation, *Phys. Rev. Lett.* **114**, 120506 (2015).
- [45] D. Gottesman, Stabilizer codes and quantum error correction, arXiv:quant-ph/9705052 (1997).
- [46] M. Hein, W. Dür, J. Eisert, R. Raussendorf, M. V. den Nest, and H. J. Briegel, Entanglement in graph states and its applications (2006), arXiv:quant-ph/0602096.
- [47] I. Schwartz, D. Cogan, E. R. Schmidgall, Y. Don, L. Gantz, O. Kenneth, N. H. Lindner, and D. Gershoni, Deterministic generation of a cluster state of entangled photons, *Science* **354**, 434 (2016).
- [48] See Supplemental Material for further details.
- [49] M. S. Tame, M. Paternostro, M. S. Kim, and V. Vedral, Quantum-information processing with noisy cluster states, *Phys. Rev. A* **72**, 012319 (2005).
- [50] M. S. Tame, M. Paternostro, M. S. Kim, and V. Vedral, An economical route to one-way quantum computation, *Int. J. Quantum Inf.* **04**, 689 (2006).
- [51] Z. Qin, W.-R. Lee, B. DeMarco, B. Gadway, S. Kotochigova, and V. W. Scarola, Quantifying entanglement in cluster states built with error-prone interactions, *Phys. Rev. Res.* **3**, 043118 (2021).
- [52] M. Horodecki, P. Horodecki, and R. Horodecki, General teleportation channel, singlet fraction, and quasidistillation, *Phys. Rev. A* **60**, 1888 (1999).
- [53] S. L. Braunstein, C. A. Fuchs, H. J. Kimble, and P. van Loock, Quantum versus classical domains for teleportation with continuous variables, *Phys. Rev. A* **64**, 022321 (2001).
- [54] S. Bose, Quantum communication through an unmodulated spin chain, *Phys. Rev. Lett.* **91**, 207901 (2003).
- [55] M. Paternostro, G. M. Palma, M. S. Kim, and G. Falci, Quantum-state transfer in imperfect artificial spin networks, *Phys. Rev. A* **71**, 042311 (2005).
- [56] M. Christandl, N. Datta, T. C. Dorlas, A. Ekert, A. Kay, and A. J. Landahl, Perfect transfer of arbitrary states in quantum spin networks, *Phys. Rev. A* **71**, 1 (2005).
- [57] S. R. White, Density matrix formulation for quantum renormalization groups, *Phys. Rev. Lett.* **69**, 2863 (1992).
- [58] N. Schuch, D. Pérez-García, and I. Cirac, Classifying quantum phases using matrix product states and projected entangled pair states, *Phys. Rev. B* **84**, 165139 (2011).
- [59] M. Dolfi, B. Bauer, M. Troyer, and Z. Ristivojevic, Multigrid algorithms for tensor network states, *Phys. Rev. Lett.* **109**, 020604 (2012).
- [60] R. Orús, A practical introduction to tensor networks: Matrix product states and projected entangled pair states, *Ann. Phys.* **349**, 117 (2014).
- [61] J. C. Bridgeman and C. T. Chubb, Hand-waving and interpretive dance: an introductory course on tensor networks, *J. Phys. A Math. Theor.* **50**, 223001 (2017).
- [62] J. Biamonte and V. Bergholm, Tensor networks in a nutshell (2007), arXiv:1708.00006.
- [63] M. Fishman, S. R. White, and E. M. Stoudenmire, The ITensor software library for tensor network calculations, *SciPost Phys. Codebases*, 4 (2022).

# Supplemental Material for “Redundant String Symmetry-Based Error Correction: Experiments on Quantum Devices”

Zhangjie Qin,<sup>1,\*</sup> Daniel Azses,<sup>2,\*</sup> Eran Sela,<sup>2</sup> Robert Raussendorf,<sup>3</sup> and V. W. Scarola<sup>1</sup>

<sup>1</sup>*Department of Physics, Virginia Tech, Blacksburg, Virginia 24061, USA*

<sup>2</sup>*School of Physics and Astronomy, Tel Aviv University, Tel Aviv 6997801, Israel*

<sup>3</sup>*Institute for Theoretical Physics, Leibniz University Hannover, 30167 Hannover, Germany*

## I. TELEPORTATION FIDELITIES

We define the graph state fidelity using measurements on all input and bulk qubits. The measurements are designed to teleport information from one end of the graph to another [1–5]. This definition of fidelity derives from the measurement-based identity gate with cluster states [1, 2]. The following compares fidelity definitions without and with noise in the input qubits.

The simplest fidelity can be constructed by starting with the input qubit that can be described by a pure state with density matrix  $\rho_{\hat{r}} = |\phi_{\hat{r}}\rangle\langle\phi_{\hat{r}}|$ . (In this section all density matrices are single-qubit density matrices.)  $\hat{r}$  is a unit vector indicating a location on the Bloch sphere. Once the input qubit is entangled with the remainder of the graph, single qubit measurements of the bulk qubits (those not at the ends) along the same direction transmits information along the graph. The bulk measurements are along the qubit- $x$  direction for the chain and diamond graphs. For the hourglass graph, the input qubit is measured in  $x$  direction and bulk qubits are along the  $y$ -direction. The output (end) qubit density matrix is  $\rho_O = |\phi_O\rangle\langle\phi_O|$ . We use quantum tomography on quantum devices to find the output density matrix.  $\rho_O$  should then be identical to the input density matrix,  $\rho_{\hat{r}}$ , in the absence of errors. We define the fidelity in the main text to be:

$$\mathcal{F}_{\hat{r}} = |\langle\phi_{\hat{r}}|U_{\Sigma}|\phi_O\rangle|^2, \quad (\text{S1})$$

where the byproduct operators  $U_{\Sigma}$  are defined in the following in the limit of no error to rotate our measurement outcome so that the output qubit orientation perfectly aligns with  $\hat{r}$  if there is no error. In the absence of error we would then retrieve  $\mathcal{F}_{\hat{r}} = 1$ .

The above definition of fidelity in terms of a pure state is sufficient to test quantum devices. To see this we can generalize the above definition to a mixed input state,  $\tilde{\rho}_{\hat{r}}$ , where the tilde indicates a non-pure density matrix due to noise on the input qubit. The input density matrix can be represented by  $\tilde{\rho}_{\hat{r}} = (\sigma^0 + \mathbf{r} \cdot \hat{\sigma})/2$  and  $\mathbf{r}$  is a Bloch sphere vector with  $|\mathbf{r}| \leq 1$ . A mixed state fidelity is then given by [6–8]:

$$\left( \text{Tr} \left[ \sqrt{(\tilde{\rho}_{\hat{r}})^{1/2} U_{\Sigma} \tilde{\rho}_O U_{\Sigma} (\tilde{\rho}_{\hat{r}})^{1/2}} \right] \right)^2 \quad (\text{S2})$$

We have checked that we retrieve identical results using either Eq. (S1) or Eq. (S2) in the experiments run on quantum devices in the main text. This shows that noise on the input and output qubits is negligible compared to other errors accumulated in our circuits.

## II. TOPOLOGICAL SYMMETRY PROTECTION AND REDUCED DENSITY MATRIX CALCULATIONS

To identify SPTO in graph states we construct and diagonalize the reduced density matrices  $\rho_A^G$  for example graphs  $G$ . The reduced density matrix is obtained from the Schmidt decomposition of pure function into equal size regions of vertex sets A and B:

$$\rho^G = |\Psi^G\rangle\langle\Psi^G|, |\Psi^G\rangle = \sum_{\nu} \lambda_{\nu} |\psi_{\nu}^B\rangle |\psi_{\nu}^A\rangle, \quad (\text{S3})$$

where  $\nu$  indexes the eigenstates and  $\lambda_{\nu}$  are the eigenvalues of the density matrix. The reduced density matrix is defined by tracing out vertices in region B:

$$\rho_A^G = \text{Tr}_B[\rho^G] = \sum_{\nu} \lambda_{\nu} |\psi_{\nu}^A\rangle\langle\psi_{\nu}^A|. \quad (\text{S4})$$

\* These authors contributed equally to this work.

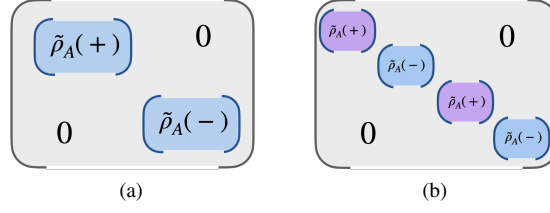


FIG. S1. *Reduced Density Matrices*: Schematic of sub-blocks of reduced density matrices of graph region A projected onto symmetry sectors,  $\tilde{\rho}_A$ , with symmetry protected topological order established by  $(\mathbb{Z}_2)^2$  (a) and  $(\mathbb{Z}_2)^4$  (b) symmetries. Examples of (a) include the chain graph state. An example of (b) includes the diamond graph state.

We then find, by direct calculation, that the reduced chain symmetries for each graph can also be diagonalized. A linear combination of eigenvectors of the reduced chain symmetries then forms a complete orthonormal basis for the reduced density matrices. The resulting reduced density matrix is then block diagonal, as shown schematically in Fig. S1. This procedure shows, on a case-by-case basis, that the degeneracies in the eigenvalues of the reduced density matrix are completely determined by the chain symmetries, as opposed to other symmetries, so long as the requisite block structure arises. The direct decomposition into sectors defined by chain symmetries will also allow us to define the order of the symmetry.

The following shows explicit example reduced density matrix calculations for the chain and diamond graphs to prove that the ideal graphs discussed in the main text are SPT states.

### 1. *Reduced Density Matrix and Reduced Symmetries: Chain Graph*

In this section we explicitly diagonalize the reduced density matrix of the 6 vertex chain graph defined by  $|\Psi_G(0)\rangle$  in the main text. We then show that the sub-block structure in the reduced density matrices (Fig. S1a) follows from reduced string symmetries.

We first trace out vertices 1, 2, and 3 of the chain (region B) to obtain the reduced density matrix for vertices in region A:

$$\rho_A^C = \sum_{\nu=1}^2 \lambda_\nu^C |\psi_\nu^C\rangle \langle \psi_\nu^C| \quad (\text{S5})$$

where

$$\begin{aligned} |\psi_1^C\rangle &= \frac{\sqrt{2}}{2} (|+\rangle_4^z |-\rangle_5^y |+\rangle_6^z + |+\rangle_4^z |+\rangle_5^y |-\rangle_6^z) \\ |\psi_2^C\rangle &= \frac{\sqrt{2}}{2} (|-\rangle_4^z |+\rangle_5^y |+\rangle_6^z + |-\rangle_4^z |-\rangle_5^y |-\rangle_6^z) \end{aligned} \quad (\text{S6})$$

and  $|\pm\rangle_i^x$ ,  $|\pm\rangle_i^y$ , and  $|\pm\rangle_i^z$  denote the eigenstates of the Pauli matrices  $X_i$ ,  $Y_i$ , and  $Z_i$ , respectively. Equations S5 and S6 show, by explicit diagonalization, that  $\rho_A^C$  has degenerate eigenvalues,  $\lambda_1^C = \lambda_2^C = 1/2$ .

We now show that the eigenstates of  $\rho_A^C$  are also eigenstates of the reduced chain symmetries. Recall from the main text that the chain graph has symmetry generators  $s_{135} = X_1 Y_3 Y_5 Z_6$  and  $s_{246} = Z_1 Y_2 Y_4 X_6$ . By tracing out the vertices in region B we obtain reduced symmetries  $Y_5 Z_6$  and  $Y_4 X_6$ . We note that the reduced symmetries do not commute. Furthermore:

$$\begin{aligned} Y_5 Z_6 |\psi_r^C\rangle &= (-1)^r |\psi_r^C\rangle \\ Y_4 X_6 |\psi_r^C\rangle &= (-1)^{r+1} i |\psi_{3-r}^C\rangle \end{aligned} \quad (\text{S7})$$

for  $r = 1$  and  $2$ .

We therefore see that we can simultaneously diagonalize  $\rho_A^C$ ,  $\text{Tr}_B[s_{246}]$ , and  $\text{Tr}_B[s_{135}]$  to uniquely determine the reduced string operators as the origin of sub-block structure and the degeneracies in the eigenvalues of  $\rho_A^C$  depicted in Fig. S1a. This calculation can be extended to longer chains. We therefore see that  $(\mathbb{Z}_2)^2$  SPTO is indicated by the degenerate eigenvalues in distinct SPT sectors.

### 2. *Reduced Density Matrix and Reduced Symmetries: Diamond Graph*

In this section we perform the same calculation as in the previous section but for the 6-vertex diamond graph to show the reduced density matrix structure found in Fig. S1b. Consider the total density matrix defining the 6-vertex diamond graph from



$|\Psi_G(0)\rangle$  in the main text. Tracing out vertices 1,2,3 in region  $B$ , we obtain the reduced density matrix for region  $A$ ,  $\rho_A^D$ . We diagonalize the reduced density matrix to find:

$$\rho_A^D = \sum_{\nu=1}^4 \lambda_\nu^D |\psi_\nu^D\rangle\langle\psi_\nu^D| \quad (\text{S8})$$

where

$$\begin{aligned} |\psi_1^D\rangle &= |+\rangle_4^z |+\rangle_5^z |+\rangle_6^x \\ |\psi_2^D\rangle &= |+\rangle_4^z |-\rangle_5^z |-\rangle_6^x \\ |\psi_3^D\rangle &= |-\rangle_4^z |+\rangle_5^z |+\rangle_6^x \\ |\psi_4^D\rangle &= |-\rangle_4^z |-\rangle_5^z |-\rangle_6^x. \end{aligned} \quad (\text{S9})$$

We therefore see four degenerate eigenvalues in the reduced density matrix,  $\lambda_1^D = \lambda_2^D = \lambda_3^D = \lambda_4^D = 1/4$ .

We now show that the eigenstates of  $\rho_A^D$  are also eigenstates of the reduced chain symmetries. Recall from the main text that the diamond graph has symmetry generators:  $s_{135} = X_1 X_3 X_5 Z_6$ ,  $s_{246} = Z_1 X_2 X_4 X_6$ ,  $s_{145} = X_1 X_4 X_5 Z_6$  and  $s_{236} = Z_1 X_2 X_3 X_6$ . Tracing out vertices 1,2, and 3 leaves the reduced symmetry generators:  $X_5 Z_6$ ,  $X_4 X_6$ ,  $X_4 X_5 Z_6$ , and  $X_6$ . We now have two symmetry groups since  $[X_4 X_5 Z_6, X_6] \neq 0$  and  $[X_5 Z_6, X_4 X_6] \neq 0$ . We can construct the eigenstates of the reduced symmetries:

$$\begin{aligned} X_6 |\psi_r^D\rangle &= (-1)^{r+1} |\psi_r^D\rangle \\ X_4 X_6 |\psi_r^D\rangle &= (-1)^{r+1} |\psi_{r+2}^D\rangle \\ X_4 X_5 Z_6 |\psi_r^D\rangle &= |\psi_{5-r}^D\rangle \\ X_5 Z_6 |\psi_{2r-1}^D\rangle &= |\psi_{2r}^D\rangle \end{aligned} \quad (\text{S10})$$

for  $r = 1$  and  $2$ .

We therefore see that we can simultaneously diagonalize  $\rho_A^D$  and the four reduced string symmetries to uniquely determine the reduced string operators as the origin of sub-block structure and the degeneracies in the eigenvalues of  $\rho_A^D$  depicted in Fig. S1b. The reduced string symmetries therefore generate  $(\mathbb{Z}_2)^4$  SPTO.

### III. BYPRODUCT OPERATORS

In this section we discuss the byproduct operators for teleportation. We begin with the diamond graph. We require that measurements on the diamond graph along the  $x$ -direction of all but the final output qubit yield  $|\phi_O^{\vec{r}}\rangle = \mathcal{H}U_\Sigma^D|\phi_I^{\vec{r}}\rangle$  where  $|\phi_I^{\vec{r}}\rangle$  and  $|\phi_O^{\vec{r}}\rangle$  are the input and output single qubit wavefunctions on vertices 1 and 6 respectively.  $\mathcal{H}$  is the Hadamard (Identity) matrix for paths with an even (odd) number of vertices on the path.

The byproduct operator choices connect to the symmetry and path we are using in the information teleportation process. Figure 1b in the main text has two paths. Label the path connecting vertices 123456 as "upper" (the path that avoids the error on link 35). And label the patch connecting vertices 124356 as the lower path (the path that encounters the error on link 35). With this convention, we construct the byproduct operator for the upper path:

$$U_\Sigma^{D^u} = (Z)^{s_2+s_4} (X)^{s_1+s_3+s_5}, \quad (\text{S11})$$

and the lower path byproduct operator:

$$U_\Sigma^{D^l} = (Z)^{s_2+s_3} (X)^{s_1+s_4+s_5} \quad (\text{S12})$$

We use these byproduct operators to define the fidelity reported in the main text.

We now turn to the hourglass graph with a bulk length  $n$ . For an even  $n$ , if we measure the input qubit in the  $x$ -direction and bulk qubits all in the  $-y$  direction, the condition  $|\phi_O^{\vec{r}}\rangle = \mathcal{H}U_\Sigma^{\text{HG}}|\phi_I^{\vec{r}}\rangle$  defines the byproduct operator. There are  $2^n$  paths we can select. When  $n$  is an even number, we choose a pair of paths and label them as upper and lower. The inset of upper

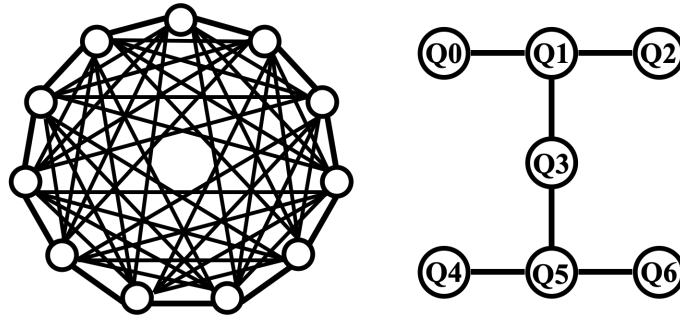


FIG. S2. *Quantum Device Geometries*: Schematics for IonQ Harmony (left) and IBMQ Nairobi (right) device qubit connectivities. The circles represent qubits and the lines indicate two-qubit gates. Gate fidelities for IBMQ and IonQ are reported in Tables I and II, respectively.

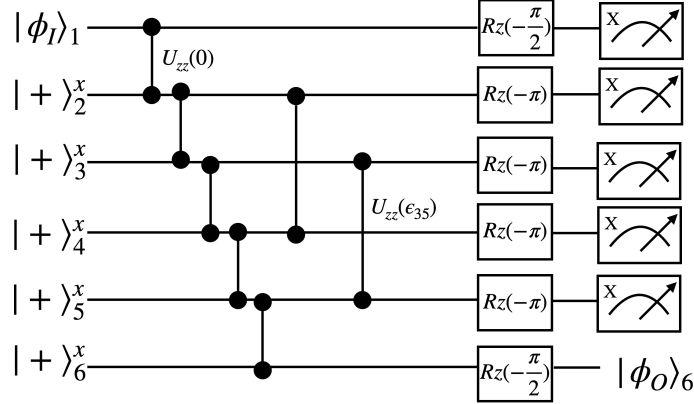


FIG. S3. *Diamond Graph Circuit Diagram*: Gate sequences used to obtain data shown in Fig. 2 (top). All but qubit 1 are first aligned along the  $x$ -direction. Qubit 1 is prepared in the state  $\phi_I$ . The qubits are then entangled with Ising gates. The gate entangling qubits 2 and 4 are perturbed by  $\epsilon_{23}$ . Single qubit  $z$ -rotations are then applied, where  $R_z(\gamma) = e^{-i\gamma Z/2}$ . Measurements of all but qubit 6 along the qubit- $x$  direction propagates the state from qubit 1 to qubit 6. Qubit 6 is measured in the basis of  $\phi_I$  to construct the fidelity.

(lower) panels of Fig. 4 in the main text show examples of an upper (lower) path for  $n = 2$ . The upper and lower path byproduct operators for  $n$  even for the hourglass graph are:

$$U_{\Sigma}^{\text{HG}^u} = (Z)^{s_{1n} + s_{(1,0)} + \dots + s_{(k-1,0)}} \times (X)^{s_1 + s_{(2,0)} + \dots + s_{(k,0)}} \quad (\text{S13})$$

and

$$U_{\Sigma}^{\text{HG}^l} = (Z)^{s_{1n} + s_{(1,1)} + \dots + s_{(k-1,1)}} \times (X)^{s_1 + s_{(2,1)} + \dots + s_{(k,1)}}, \quad (\text{S14})$$

respectively. Here  $s_{(i,j)}$  labels measurement outcomes on bulk vertex  $(i, j)$  in Fig. 3 in the main text.  $s_1$  labels the input vertex.

#### IV. QUANTUM CIRCUITS AND QUANTUM DEVICE PARAMETERIZATION

The diamond and hourglass graph states discussed in the main text were implemented on two different quantum devices, IBMQ Nairobi and IonQ Harmony. Teleportation experiments of input states across the graphs were then performed. Fig. S2 shows schematics of the qubit connectivity for both devices.

Figures S3 and S4 show the quantum circuits used to prepare the graph states. Initialization along the qubit- $x$  direction is followed by entangling Ising gates. The  $z$  and  $x$ -rotations were performed to set up the appropriate measurement bases. The final measurements implement teleportation along the graph states, from qubit 1 to qubit 6.

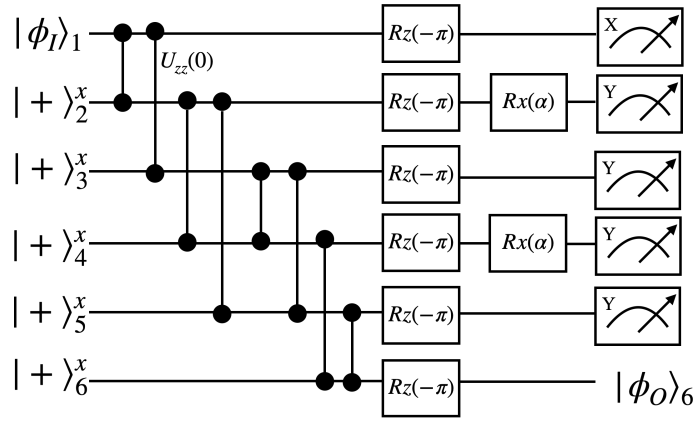


FIG. S4. *Hourglass Graph Circuit Diagram*: The same as Fig. S3 but used for the hourglass graph with final qubit measurements along the  $x$ -direction. Single qubit  $x$ -rotations are then applied, where  $R_x(\alpha) = e^{-i\alpha X/2}$ .

Qubit	T1 ( $\mu$ s)	T2 ( $\mu$ s)	F (GHz)	A (GHz)	RA ( $\times 10^{-2}$ )	M0P1	M1P0	RL (ns)	ID ( $\times 10^{-4}$ )	SX ( $\times 10^{-4}$ )	PX ( $\times 10^{-4}$ )	CN ( $\times 10^{-3}$ )	GT (ns)
Q0	107.5	28.11	5.26	-0.33983	2.140	0.0284	0.0144	5560.889	3.282	3.282	3.282	0-1:7.243	248.889
Q1	137.77	67.82	5.17	-0.34058	2.310	0.0294	0.0168	5560.889	2.873	2.873	2.873	1-3:1.078	270.222
Q2	85.88	96.75	5.274	-0.3389	4.010	0.0626	0.0176	5560.889	2.406	2.406	2.406	2-1:7.034	391.111
Q3	77.05	48.93	5.027	-0.34253	6.350	0.088	0.039	5560.889	5.493	5.493	5.493		
Q4	111.79	75.6	5.177	-0.34059	2.050	0.031	0.01	5560.889	2.625	2.625	2.625	5-4:6.453	277.333
Q5	119.8	18.5	5.293	-0.34053	2.280	0.0294	0.0162	5560.889	3.202	3.202	3.202	5-3:2.101	241.778
Q6	113.77	114.03	5.129	-0.34044	2.080	0.035	0.0066	5560.889	2.325	2.325	2.325	6-5:7.750	305.778

TABLE I. Calibration data of the IBM device backend, *ibm\_nairobi*, used to generate the real-device simulation data. Abbreviations are defined as follows: F = frequency, A = anharmonicity, RA = readout assignment error, M0P1 = probability of measurement 0 and preparation 1, M1P0 = probability of measurement 1 and preparation 0, RL = readout length, SX =  $\sqrt{X}$  error, PX = Pauli-X error, CN = CNOT error, GT = gate time.

The real quantum device data presented in the main text are averages obtained using 10000 (100) shots on IonQ for the diamond (hourglass) graph, and 8192 shots on IBMQ. The standard deviation in Gaussian fits are about 0.05 and 0.1 for IonQ and on IBMQ, respectively.

Qubit	T1 (s)	T2 (s)	GT-1Q(s)	GT-2Q(s)	RT(s)	RS(s)	F-1Q	F-2Q	SPAM
Q0-10(Mean)	10000	0.2	0.00001	0.0002	0.00013	0.0002	0.9986	0.9726	0.99752

TABLE II. Calibration data of the IonQ device backend, used to generate the real-device simulation data. Abbreviations are defined as follows: GT-1Q= single qubit gate time, GT-2Q= two qubit gate time, RT=readout time, RS=reset time, F-1Q= single-qubit gate fidelity, F-2Q=two-qubit gate fidelity, SPAM=state preparation and measurement fidelity

The data are significantly impacted by noise beyond the unitary noise sources discussed in the main text. These noise sources suppress the fidelity beyond our analysis. Tables I and II show device parameters from the quantum devices used to create the data shown in the main text.

We model the noise on the IonQ device. Table II shows that two-qubit gate fidelity is lowest. The native two-qubit gates in the IonQ device [9] are Mølmer-Sørensen Ising-based gates. We model non-unitary perturbations using two-qubit gate depolarizing noise defined in the Qiskit noise model [10]. We use the two-qubit depolarizing channel as a proxy for cumulative error due to a variety of non-unitary noise sources [9, 11].

Figure S5 compares real device teleportation experiments with simulation. In the classical simulations, we choose two different two-qubit depolarizing noise probabilities to bound the quantum device data. We see that the real device data points (red circles) lie between simulator results (upward and downward triangles) which captures the qualitative effect of noise seen on the real device. We therefore conclude that two-qubit depolarizing noise serves as a good model for the dominant noise channel which, in turn, lowers the teleportation fidelity for IonQ Harmony from the ideal values discussed in the main text.

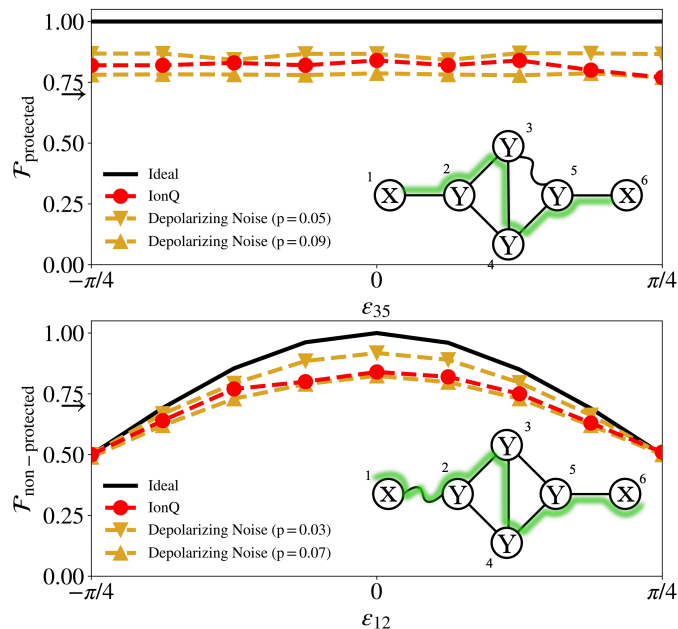


FIG. S5. The same as the IonQ data in Fig. 2 in the main text but with classical noise-model simulations included (triangular symbols). The classical noise-model simulations include a calculation of the fidelity with depolarizing noise applied to two-qubit gates used to build the graph state. The fidelity is measured using the initial qubit aligned along the  $+z$  direction.  $p$  is the probability of the two-qubit depolarizing noise [10]. The qualitative accuracy between the noise model and the real machine data indicate that two-qubit depolarizing noise offers a good model for non-unitary perturbations found on IonQ.

## V. MBQC PROTOCOL PATH CALIBRATION

In this section we describe the calibration process of finding the correct path to use and how to find on what sites the errors occur. We focus on 1-qubit error here as 2 errors may block both paths, reducing the fidelity of the teleportation. We further assume, as in other noisy quantum device error mitigation techniques, that the errors do not change drastically from the calibration process to the actual experiment.

Let us focus on the case of Fig. 3 in the main text. Here we have the upper path and the lower path, where one path is broken but we do not know which. To find the broken path we teleport a simple known state such as  $|0\rangle$  or  $|+\rangle$ , as those do not require tomography or different quantum measurements for the paths, and use the byproduct operators of both paths on the output to get two bits  $s_{\text{out}}^{\text{upper}}$ ,  $s_{\text{out}}^{\text{lower}}$ , each for its respective path. In the case of no errors, both should be 0, indicating perfect fidelity, however, as one path is erroneous the fidelity will not be perfect. On a real quantum computer, it may be that both paths contain some errors, but one path has decreased fidelity with respect to the other one (*i.e.* 90% vs 60% fidelity). Hence, we calibrate the quantum computer to the best path using the average fidelity over the simple quantum states. Additionally, we may use tomography and sample input states randomly to have better sampling. Therefore, in the case of a single erroneous path the calibration method always finds the correct path.

## VI. MATRIX PRODUCT STATE SIMULATIONS AND SYMMETRIC PERTURBATIONS

In this section we explain the details of the MPS calculations. MPS calculations scale with system size only polynomially, thus, they are preferred for large system sizes. Here we check symmetric perturbations and demonstrate that both SOP and teleportation fidelity remain unaffected by them, as shown in previous works [12].

We focus on a simple 1-qubit perturbation, but the analysis and methods are general. The hourglass graph state, depicted in Fig. 3 in the main text when ignoring the left-most qubit, is perturbed by adding the following symmetry preserving terms

$$H_Y = -\cos \alpha \left[ \sum_{j=1}^L K_j \right] - \sin \alpha \left[ \sum_{i=1}^n (Y_{i,0} + Y_{i,1}) \right],$$

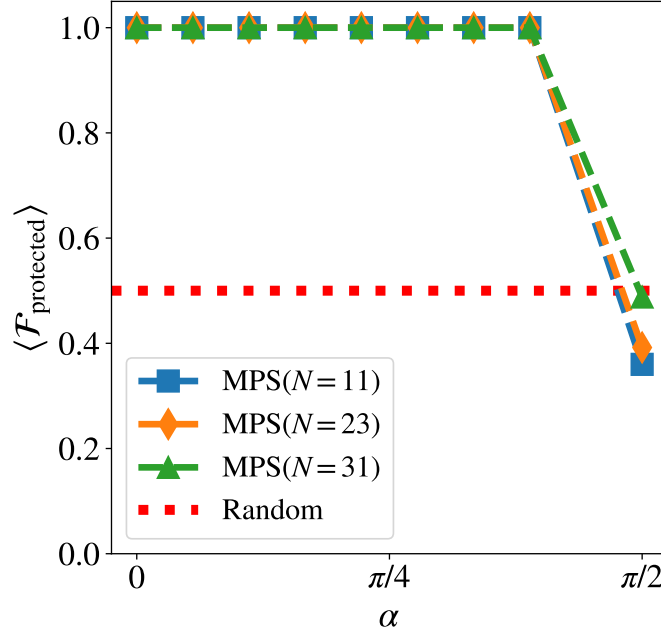


FIG. S6. The MBQC teleportation fidelity for the upper path in the hourglass graph, which is the path that protects the MBQC teleportation protocol. The calculations were done using MPS of size  $N = L + 1$  for 25 random input states with 10 measurements each as explained in the text. The results show the protection of the teleportation protocol for  $\alpha \neq \pi/2$  as the teleportation is performed perfectly for any input state. Due to convergence problems of the bond dimension, we excluded one point near  $\pi/2$  as the ground state convergence required computational resources that exceeded those of a regular computer for  $N > 11$ .

where  $L = 2n + 2$  representing the upper and lower row, each of size  $n$ , and the qubits at their left and right endpoints notated  $m$ ,  $o$  respectively ( $m$  and  $o$  are the abbreviations of middle and output respectively). The input qubit is still not added in this stage. As a result, for  $\alpha = 0$  the ground state is the usual entangled graph state, but as  $\alpha$  increases the graph state is distorted. A phase transition occurs at  $\alpha_c = \pi/4$  where the state is no longer SPT for  $\alpha > \alpha_c$ . However, perfect teleportation is still possible as long as the symmetry is left unbroken. Therefore, only the point  $\alpha = \pi/2$  is an exception as it breaks the entanglement completely, destroying the correlations between the input and the output qubits.

This ground state is constructed for any  $\alpha$  using MPS since we find MPS to be an excellent approximation to the true ground state. This ground state is now used as the resource state for our MBQC protocol as follows:

1. The initial MPS is obtained by coupling an input state. The input state is chosen randomly in the XY plane. This is done by rotating it by random  $\phi$  around  $Z$ . For example, in Fig. 5 in the main text we use 75 random states in the XY plane with 100 measurements each. It is then entangled with a CZ gate at the left link, see Fig. 1b in the main text.
2. We apply a rotation on every qubit in the MPS according to the measurements (i.e. For X [Y] measurements we apply  $H$  [ $HS^\dagger$ ] gate), except for the output.
3. We now sample the MPS, excluding the output, in the computational basis by applying the projectors according to the measurements probabilities. This results in measurement results  $s_i = 0, 1$  for the qubit  $i$ , where  $s_{\text{in}}$  is the result for the input qubit.
4. The output is measured in two steps. First we rotate around  $Z$  by an angle  $(-1)^{1+l}\phi$ , which corrects the  $X$  byproduct operator, where the sign is path dependent  $l_{\text{upper}} = s_m + \sum_k s(2k,0)$ ,  $l_{\text{lower}} = s_m + \sum_k s(2k,1)$ . Then, a simple measurement in the  $X$  direction follows by applying  $H$  and the result is  $s_o$ .
5. We expect to get  $s_o = 0$ , but that is only if there were no  $Z$  byproduct operators that flip the result (in the  $X$  basis). Thus, a flip is needed in the case of a  $Z$  byproduct operator. This depends on the path, hence, we flip if  $l = 1 \pmod{2}$ , where  $l_{\text{upper}} = s_{\text{in}} + \sum_k s(2k-1,0)$ ,  $l_{\text{lower}} = s_{\text{in}} + \sum_k s(2k-1,1)$  are the  $l$  for their respective paths. After flipping, the result is  $s_o = 0$  if the MBQC teleportation protocol was successful.

Let us now describe the MPS results. The results are shown in Fig. S6. For each  $\alpha$  we generated a resource state. Each point corresponds to 25 random input states that we run its MBQC protocol 10 times. The average over the random states and the

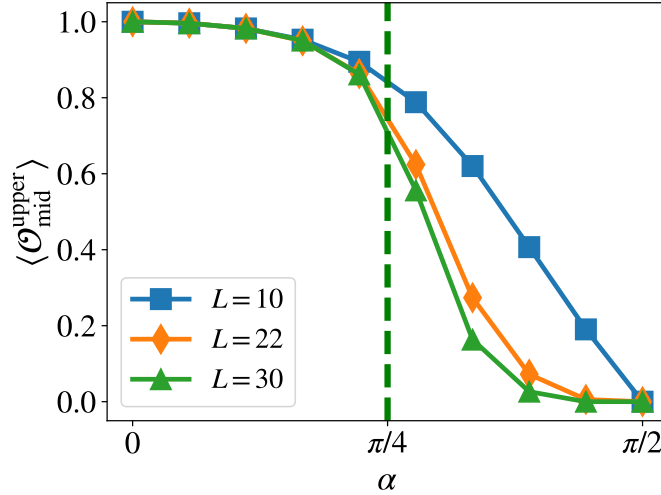


FIG. S7. The SOP,  $\langle \mathcal{O}_{\text{mid}}^{\text{upper}} \rangle$ , of the upper path plotted for the hourglass resource states used for the MBQC teleportation protocol (without an input qubit) in the presence of symmetric noise. The phase transition at  $\alpha_c = \pi/4$  is sharp in the limit  $L \rightarrow \infty$ , indicating that the computational power for rotations disappears for  $\alpha > \alpha_c$ .

runs converges to the fidelity of the MBQC protocol, which is the success probability to teleport random input state. Our MPS calculations show that that fidelity using unperturbed paths is unity for all converged MPS data, except the unentangled point  $\alpha = \pi/2$ .

We now continue to calculate the SOPs underlying computational power, which includes rotations. As we discussed, a phase transition at  $\alpha_c = \pi/4$  eliminates the SPT nature as the resource state undergoes phase transition. To detect the SPT nature we consider the SOP, which in this case given by

$$\mathcal{O}_{\text{mid}}^{\text{upper}} = s_o \prod_{k \geq l} s_{(l,0)} = Z_{(l-1,0)} Z_{(l-1,1)} \left( \prod_{L > k \geq l} Y_k \right) X_o, \quad (\text{S15})$$

where  $l = L - 4 \lfloor L/8 \rfloor$  and  $X_o$  acts on the rightmost qubit, which is the output for the MBQC protocol.  $l$  ensures that we focus on the SOP of the upper path. The results are given in Fig. S7. It is clear the for  $\alpha = 0$  we get  $\mathcal{O}_{\text{mid}}^{\text{upper}} = 1$  as it is a multiplication of stabilizers. When  $\alpha = \alpha_c$  a phase transition causes the SOP to decrease sharply to 0. In the limit  $L \rightarrow \infty$  the SOP is greater than 0 at the SPT phase and it is 0 in the trivial phase, indicating the SPT phase transition. Therefore, as the SOP is deeply linked to the computational power, it is clear that the computational power vanishes for  $\alpha > \alpha_c$  for general 1-qubit gates. However, the MBQC teleportation, which is the identity gate, still remains intact.

## VII. STRING ORDER PARAMETER FOR SYMMETRY BREAKING PERTURBATIONS

In this section we complete the picture by demonstrating the diminishing computational power when breaking the symmetry from the SOP. As in the last section, we consider the resource state derived from the Hamiltonian

$$H_Z = -\cos \alpha \left[ \sum_{j=1}^L K_j \right] - \sin \alpha \left[ \sum_{i=1}^n (Z_{i,0} + Z_{i,1}) \right], \quad (\text{S16})$$

where  $L = 2n + 2$  and the qubits and  $n$  are as in Fig. 3 in the main text, excluding the input qubit, which is the left most qubit. The SOP is given in Eq. S15. The MPS calculations as explained in the last section are presented in Fig. S8. As the system size grows the SOP diminishes to 0 very fast, indicating that the perturbation destroys the inherent computational power of the resource state even for small  $\alpha$ . We expect that in the limit of  $L \rightarrow \infty$  the SOP will decrease exponentially fast with increasing  $\alpha$ . Therefore, the SPT nature, and thus the computational power, is present only when non-symmetric perturbations

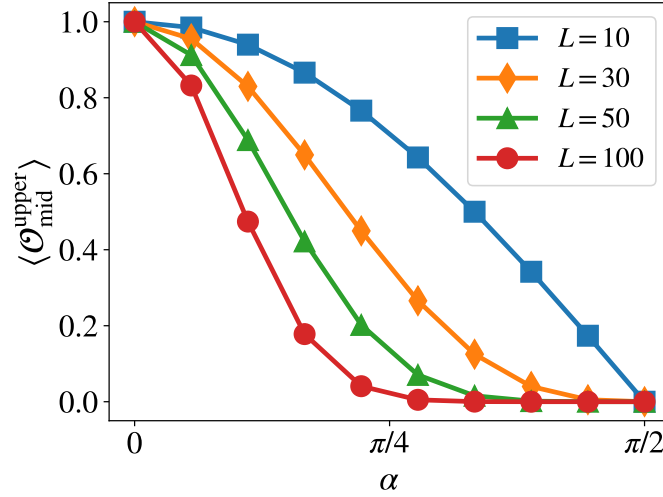


FIG. S8. The SOP,  $\langle \mathcal{O}_{\text{mid}}^{\text{upper}} \rangle$ , of the upper path plotted for the hourglass resource states used for the MBQC teleportation protocol (without an input qubit) in the presence of non-symmetric noise. As  $L$  increases, the computational power diminishes faster and completely vanishes for smaller  $\alpha$ . This indicates that in the limit  $L \rightarrow \infty$  we may have no computational power even for any  $\alpha > 0$  as it seems to vanish exponentially fast.

are negligible.

- 
- [1] R. Raussendorf and H. J. Briegel, A one-way quantum computer, *Phys. Rev. Lett.* **86**, 5188 (2001).
  - [2] R. Raussendorf, D. E. Browne, and H. J. Briegel, Measurement-based quantum computation on cluster states, *Phys. Rev. A* **68**, 022312 (2003).
  - [3] M. S. Tame, M. Paternostro, M. S. Kim, and V. Vedral, Quantum-information processing with noisy cluster states, *Phys. Rev. A* **72**, 012319 (2005).
  - [4] M. S. Tame, M. Paternostro, M. S. Kim, and V. Vedral, An economical route to one-way quantum computation, *Int. J. Quantum Inf.* **04**, 689 (2006).
  - [5] Z. Qin, W.-R. Lee, B. DeMarco, B. Gadway, S. Kotochigova, and V. W. Scarola, Quantifying entanglement in cluster states built with error-prone interactions, *Phys. Rev. Res.* **3**, 043118 (2021).
  - [6] A. Uhlmann, The “transition probability” in the state space of a \*-algebra, *Reps. on Math. Phys.* **9**, 273 (1976).
  - [7] R. Jozsa, Fidelity for mixed quantum states, *Jour. of Mod. Optics* **41**, 2315 (1994).
  - [8] Y.-C. Liang, Y.-H. Yeh, P. E. M. F. Mendonça, R. Y. Teh, M. D. Reid, and P. D. Drummond, Quantum fidelity measures for mixed states, *Reps. on Prog. in Phys.* **82**, 076001 (2019).
  - [9] K. Wright, K. M. Beck, S. Debnath, J. M. Amini, Y. Nam, N. Grzesiak, J.-S. Chen, N. C. Pimenti, M. Chmielewski, C. Collins, *et al.*, Benchmarking an 11-qubit quantum computer, *Nat. Commun.* **10**, 5464 (2019).
  - [10] Qiskit contributors, Qiskit: An open-source framework for quantum computing (2023).
  - [11] Y. Wu, S.-T. Wang, and L.-M. Duan, Noise analysis for high-fidelity quantum entangling gates in an anharmonic linear Paul trap, *Phys. Rev. A* **97**, 062325 (2018).
  - [12] D. Azses, R. Haenel, Y. Naveh, R. Raussendorf, E. Sela, and E. G. Dalla Torre, Identification of symmetry-protected topological states on noisy quantum computers, *Phys. Rev. Lett.* **125**, 120502 (2020).